Numerical investigation of the coupled interaction between an unsteady aerodynamic flow field and a water film coating on a circular cylinder.

I J Taylor [1,*], A C Robertson [2]

[1] *Department of Mechanical and Aerospace Engineering, University of Strathclyde, Glasgow, Scotland, G1 1XJ, UK*

[2] *East Kilbride Engineering Services (EKES), Kelvin Building, Scottish Enterprise Technology Park, East Kilbride, Scotland, G75 0RD, UK.*

ABSTRACT

Rain-wind induced vibration is an aeroelastic phenomenon that occurs on the inclined cables of cable-stayed bridges and arises due to the interaction between the unsteady wind loading and the formation of water rivulets on the cable surface. A new numerical method has been developed at the University of Strathclyde to simulate the influence of the external flow field on the rivulet dynamics and vice versa. The approach is to couple a Discrete Vortex Method solver to determine the external flow field and unsteady aerodynamic loading, and a pseudo-spectral solver based on lubrication theory to model the evolution and growth of the water rivulets on the cable surface under external loading. Results of this coupled model are presented, to provide detailed information on the development of water rivulets and their interaction with the aerodynamic field. In particular, the effect of the initial water film thickness and the angle of attack in plane on the resulting rivulets are investigated. The results are consistent with previous full scale and experimental observations with rivulets forming on the upper surface of the cable only in configurations where rain-wind induced

[*] Corresponding author : Department of Mechanical and Aerospace Engineering, James Weir Building, Montrose Street, University of Strathclyde, Glasgow, G1 1XJ, UK.

Tel.: +44 (0)141 548 3753; *Email address* : ian.taylor@strath.ac.uk

vibration has been observed. Additionally, the thickness of the lower rivulet is found to be self-limiting in all configurations. The results demonstrate that the model can be used to enhance the understanding of the underlying physical mechanisms of rain-wind-induced vibration.

KEYWORDS : Rain-wind induced vibration; Cables; Computational wind engineering; Rivulet.

1. INTRODUCTION

Rain-Wind Induced Vibration (RWIV) is now accepted as a distinct aeroelastic phenomenon that can occur on the inclined cables of cable stayed bridges. The large amplitude oscillations this causes are widely thought to arise due to the three way interaction between unsteady aerodynamic loading, rivulets of rain water running down the surface of the cable and the structural dynamics of the cable.

First formally reported by Hikami and Shiraishi (1988), who recorded the strong influence of rain on large amplitude cable oscillations during the construction period for the Meikonishi Bridge. Since this event there have been numerous observations and investigations of RWIV. Notable amongst these are those undertaken on the Erasmus Bridge by Geurts et al. (1998), the Fred Hartman Bridge by Zuo et al. (2008) and the Dongting Lake Bridge by Ni et al. (2007).

In an attempt to gain a satisfactory understanding of the underlying physical mechanism of the instability, RWIV, has been the subject of a large amount of international research activity. These have utilized a variety of techniques and include, full scale investigations of RWIV events on bridges, as highlighted above (Zuo et al. 2008; Ni et al. 2007) and a range of wind tunnel experiments to ascertain particular aspects of the phenomenon, notably Matsumoto et al. (2003), Flamand (1995), Verwiebe and Ruscheweyh (1998), Bosdogianni and Olivari (1996) and Gu and Du (2005). Although much progress has been made, due to the complexity of the coupled

interaction between the rain water, wind and cable, a complete understanding of this phenomenon is yet to be obtained.

The data obtained from various researchers, thus far, has determined a range of conditions under which the RWIV phenomenon is most likely to occur. This can be summarised as typically being between wind speeds of 5 and 15 m/s, corresponding to Reynolds numbers, Re, of between 5×10^4 and 1.5×10^5 and reduced velocities U_R of between 20 and 90, where Re is based on the wind speed normal to the cable and the cable diameter, and U_R is defined by $U_R = U_\infty/fD$ (Cosentino et al. 2003; Matsumoto et al. 1995).

Moderate rainfall is required (Hikami and Shiraishi 1988) though it is difficult to ascertain a consistent definition of “moderate” rain from the published research. Indeed many studies have not measured exact rainfall or water flow rates. Furthermore on a number of occasions, vibrations have been identified as RWIV despite having occurred under dry conditions. It is postulated that due to this difference in the precipitation conditions, that these “dry” vibrations are due to a different but related physical phenomenon, such as vortex induced vibration at high reduced velocity (Matsumoto et al. 2001) or dry-inclined galloping (Macdonald and Larose, 2008). Zuo et al. (2008) also present analysis of full scale data that suggests that RWIV might be due to a vortex-induced type of excitation that is different from the classical Karman vortex shedding.

Using the angles of inclination in the cable pylon plane, α, and yaw angle, β, as displayed in the configuration of stay cable geometry in Fig. 1, it can be said that RWIV typically occurs in cables which descend in the windward direction, at yaw angles between $20° \leq \beta \leq 60°$ (Cosentino et al. 2003; Flamand 1995), and at angles of inclination between $20° \leq \alpha \leq 45°$ (Hikami and Shiraishi 1988; Gu and Du 2005). Although vibrations have also been noted in near vertical hangers ($\alpha \simeq 90°$) (Ruscheweyh and Verwiebe 1995) and cables which ascend in the windward direction

($\beta < 0°$) (Zuo and Jones 2003) these are again thought to result from a different mechanism (Cosentino et al. 2003).

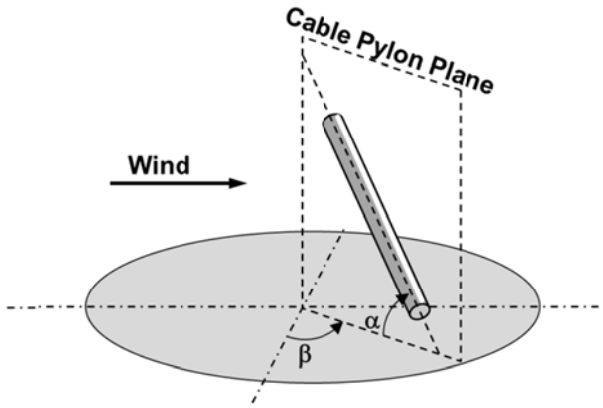

Figure 1. Definition of orientation of stay cable system geometry : Cable-pylon plane, angle of inclination (α) and angle of yaw (β).

The cables which undergo vibration are typically found to fall within the diameter range 100mm ≤ D ≤ 250mm (Cosentino et al. 2003; Matsumoto et al. 1992), to have low structural damping, $\zeta \leq 0.5\%$ (Geurts et al. 1998; Gu and Du 2005) and to be coated in Polyethylene (Flamand 1995; Matsumoto et al. 1992). Likewise the response has typically been found to occur in the frequency range 0.6 to 3 Hz (Matsumoto et al. 1992), to occur in more than one mode (Zuo et al. 2008) and to vibrate at an angle aligned to the cable-pylon plane (Fig. 1). The magnitude of this vibration, although amplitude limited, is significant with peak to peak responses of up to 2 m being reported corresponding typically to amplitude to diameter ratios, a/D, of between 1.0 and 2.0 (Matsumoto et al. 1992).

Environmental conditions should present flow with low free-stream turbulence and that is well aligned with the ground (Cosentino et al. 2003; Matsumoto et al. 1992). Certain studies (Flamand 1995) also suggest that the cables themselves should be

sufficiently coated in contaminant or pollution to make the cable surface less hydrophobic, thus making the formation and oscillation of rivulets more likely.

Indeed it has been established that the presence and location of the rivulets of rain water on the surface of the cable is one of the key aspects of the RWIV instability. Experimental results have shown that under the incident conditions most likely to cause RWIV, the thin film of rain water present on the cable typically accumulates to form two rivulets, one each on the upper leeward side and lower windward side respectively (Fig. 2). Furthermore it is the former which is largely responsible for the vibration (Flamand 1995; Bosdogianni and Olivari 1996).

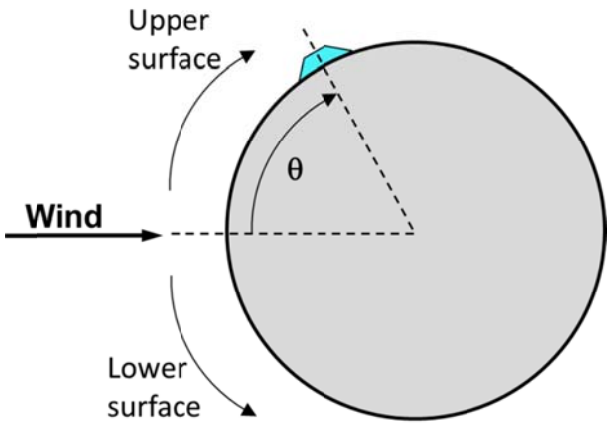

Figure 2. Definition of orientation of rivulet location on the cable surface : Rivulet angle, θ, clockwise from windward horizontal.

To identify the effect of the rivulets on the external aerodynamic field and vice versa, other studies have concentrated on specific aspects of the location and dynamics of the rivulet motion. These investigations can be broadly separated into two distinct classes, those where the rivulet is replaced by a fixed, static, rigid protuberance, i.e. an 'artificial rivulet' (Matsumoto et al. 1995; Bosdogianni and Olivari 1996) and those where a film of water is sprayed onto the surface of the cable and the rivulets are allowed to form 'naturally' (Flamand 1995; Cosentino et al. 2003; Verwiebe

and Ruscheweyh 1998; Gu and Du 2005; Wang et al. 2005). Both classes indicate that it is the presence of the rivulet on the upper surface which is largely responsible for the vibration (Matsumoto et al. 1995), while the latter class also indicates that when free to do so, the rivulets oscillate circumferentially at the same frequency as that with which the cable vibrates. Differentiating between the effect of circumferential oscillation and rivulet position in the 'artificial rivulet' investigations has, however, proven more difficult and led to discrepancies in the literature. In particular Verwiebe and Ruscheweyh (1998) determined that the circumferential oscillation of the rivulet is a primary cause of RWIV, whereas Bosdogianni and Olivari (1996) suggest that it is rivulet location and not its profile or circumferential oscillation which initiates the response. Chen et al. (2013) present a set of detailed measurements of the development of rivulets from an artificial rainfall wind tunnel test. The experiments use an ultrasonic transmission thickness measurement system to provide a nonintrusive measurement of the rivulet profile, allowing a much higher resolution of the spatial and temporal variation of the rivulets.

Several analytical models have also been developed to investigate RWIV. Most are loosely based on the work of Yamaguchi (1990), wherein the RWIV mechanism is modelled as a two-dimensional, multiple mass, multiple degree of freedom (DOF), spring mass damper system, with aerodynamic forces determined using a quasi-steady approximation. These analytical models share several common features, but also present distinct differences determined by the exact nature of the specific aspect under investigation, two such examples being a 2DOF model with a circumferentially movable rigid attachment representing the 'artificial rivulet' (Gu and Huang 2008), and a 4DOF three mass model to investigate the differences between laminar and turbulent flow on the cable-rivulet system response (Peil and Dreyer 2007).

Despite all of this analytical work, however, computational models for RWIV are scarce due to the complexity of the problem and the need to couple models for the thin

film of rain water, the unsteady aerodynamic field, and the structural dynamics of the cable. To date, the majority of the numerical investigations of RWIV have instead focused on fixed rigid artificial rivulets, with 2D and 3D large eddy simulations (LES) examining the effect that static rivulets have on the overall flow field (Li and Gu 2006; Liu et al. 2007). That said, Lemaitre et al. (2007) presented a different approach which uses lubrication theory and the time averaged flow-field over a circular cylinder to ascertain the evolution of the rain water rivulets.

Recent research at the University of Strathclyde has focused on developing a numerical model to investigate aspects of RWIV. The approach adopted couples a modified, pre-existing unsteady aerodynamic solver for the external aerodynamic flow field with a solver based on a thin-film model for the evolution and deformation of the water rivulets. The thin-film approach used for the rivulet model is similar to that used by Lemaitre et al. (2007). Details of the development and validation of the rivulet model along with results of the effect of various aerodynamic loadings on the rivulet evolution and growth are presented in detail in Robertson et al. (2010). Results from the fully coupled aerodynamic and thin film model are presented in Taylor and Robertson (2011), which provides a detailed discussion of the development of the water film under the action of unsteady aerodynamic loading, and highlight aspects of the results that may contribute to the physical mechanism of the aeroelastic phenomenon.

The research presented in the current paper provides new results from the coupled solver for a range of configurations. In particular, the effect of varying film thickness on the rivulet evolution and the variation of angle of attack in plane is presented. The latter of these, the angle of attack in plane, γ_θ, (defined in Appendix A) is a variable that is constructed such that the three-dimensionality of a yawed inclined cable can be represented in two-dimensions. The results presented herein provide further verification of the methodology used in the numerical model. It is anticipated

that the coupled model presented will provide useful information to help in the development of a better understanding of the underlying RWIV mechanism. On-going and future research will be focussed on the development of a 3D solver for RWIV and also on investigating the effect of cable oscillation on the rivulet formulation and evolution. In particular, the effect of the low reduced frequency oscillation, characteristic of galloping type motion are currently under investigation and will be reported in the near future.

NOMENCLATURE

a	amplitude of cable vibration
B	solid body in unsteady aerodynamic solver
D	diameter of cable / cylinder
F	flow field in unsteady aerodynamic solver
f	body oscillation frequency
g	acceleration due to gravity
h	thickness of water film on surface of cylinder
$\mathbf{i}, \mathbf{j}, \mathbf{k}$	unit orthogonal vectors
$\mathbf{n}, n$	unit vector and distance normal to body surface
P	pressure distribution
R	radius of cylinder
Re	Reynolds number $= UD/\nu$
$\mathbf{r}$	position vector
S	surface of body in unsteady aerodynamic solver

$\mathbf{s}$, s unit vector and distance tangential to body surface

T shear distribution

t time

$\mathbf{U}$, U velocity vector and magnitude

U_R reduced velocity ($= U_\infty/fD$)

α cable inclination angle

β cable yaw angle (angle of cable to wind direction)

γ surface tension of water

γ_θ angle of attack in plane

ζ damping ratio

θ angle around circumference of cylinder

μ dynamic viscosity of fluid

ν kinematic viscosity of fluid

ρ density of fluid

$\mathbf{\Psi}$, Ψ vector potential and stream function

$\mathbf{\Omega}$, Ω rotational velocity of solid body, vector and magnitude

$\boldsymbol{\omega}$, ω vorticity vector and magnitude

Subscripts

∞ freestream; far field

ac anti-clockwise around cylinder surface

eff effective value

i denotes number of the body under consideration (for this study with a single body, will always ≡ 1)

ic Denotes reference point for the body.

p point within flow or on body surface.

w water.

0 initial value.

$$\frac{D\mathbf{x}}{Dt} = \frac{\partial \mathbf{x}}{\partial t} + (\mathbf{x}.\nabla)\mathbf{x}$$ Material derivative of vector **x**

2. COUPLED NUMERICAL MODEL

The numerical approach used in the model for RWIV is to couple a modified version of an already existing unsteady aerodynamic solver for the external aerodynamic flow with a solver based on a thin-film model for the evolution and deformation of the water rivulets. Each model was separately developed and has been reported previously (Taylor and Vezza, 1999, 2001; Robertson et al., 2010), however brief details of each model and the approach used in the coupled solver are now presented.

2.1. Aerodynamic Model

The two-dimensional discrete vortex method used for this analysis is a modified version of the DIVEX code developed at the Universities of Strathclyde and Glasgow (Taylor and Vezza, 1999, 2001). DIVEX has previously proven successful with unsteady, incompressible, highly separated flows such as those under investigation (Taylor and Vezza, 1999). For the RWIV phenomenon in particular, an extensive

investigation into the effects of artificial rivulets on the unsteady aerodynamic flow field, similar to experimental investigations (Matsumoto et al., 2007), has been successfully undertaken. The results highlighted the importance of the location of the rivulet on the cylinder surface, and the potential for galloping instabilities for certain configurations (Taylor et al., 2010).

The numerical technique utilised by vortex methods is based on the discretisation of the vorticity field rather than the velocity field, into a series of vortex particles (Taylor and Vezza, 1999; Lin et al., 1997). These particles, of finite core size, each carry a certain amount of circulation, and are tracked throughout the flow field they collectively induce. As such, the model does not require a calculation mesh providing a very different approach to more traditional grid based computational fluid dynamics methods. One of the main advantages of vortex methods, is that their Lagrangian nature significantly reduces some of the problems associated with grid methods, such as numerical diffusion and difficulties in achieving resolution of small scale vortical structures in the flow. A detailed review of the key fundamental aspects and numerical features of vortex methods is provided by Sarpkaya (1989).

2.1.1. Mathematical Formulation

Two dimensional incompressible viscous flow is governed by the vorticity-stream function form of the continuity and Navier-Stokes equations (1) and (2) :

Continuity equation :

$$\nabla^2 \Psi = -\omega \qquad (1)$$

Vorticity transport equation :

$$\frac{\partial \boldsymbol{\omega}}{\partial t} + (\mathbf{U}.\nabla)\boldsymbol{\omega} = \nu \nabla^2 \boldsymbol{\omega} \qquad (2)$$

where the vorticity vector, $\boldsymbol{\omega}$, is defined as the curl of the velocity (3) and $\boldsymbol{\Psi}$ is a vector potential defined by (4)

$$\boldsymbol{\omega} = \nabla \times \mathbf{U} \quad \text{with} \quad \boldsymbol{\omega} = \omega \mathbf{k} \qquad (3)$$

$$\mathbf{U} = \nabla \times \boldsymbol{\Psi}, \quad \nabla \boldsymbol{\Psi} = 0 \quad \text{with} \quad \boldsymbol{\Psi} = \Psi \mathbf{k} \qquad (4)$$

The vorticity transport equation (2) defines the motion of vorticity in the flow due to convection and diffusion. As the pressure field is not explicitly defined in (2), the variation of vorticity at a point in the flow is therefore influenced by the surrounding flow velocity and vorticity.

The calculations are subject to the far field boundary conditions (5) and the no-slip and no-penetration conditions at the surface of the body (6).

$$\mathbf{U} = \mathbf{U}_\infty \quad \text{or} \quad \nabla \Psi = \nabla \Psi_\infty \quad \text{on} \quad S_\infty \qquad (5)$$

$$\mathbf{U} = \mathbf{U}_i \quad \text{or} \quad \nabla \Psi = \nabla \Psi_i \quad \text{on} \quad S_i \qquad (6)$$

The velocity at a point **r** on the surface or within body *i* is described by :

$$\mathbf{U}_i = \mathbf{U}_{ic} + \boldsymbol{\Omega} \times \left(\mathbf{r}_p - \mathbf{r}_{ic}\right) \qquad (7)$$

where $\mathbf{r}_{ic}$ is a fixed reference point on the body. This may also be represented in stream function form by

$$\nabla^2 \Psi = -2\Omega_i \quad \text{in body } B_i \qquad (8)$$

To enable the evaluation of the velocity influence on the flow due to the moving body, the solenoidal velocity field is also applied within body B_i. The solenoidal property of the velocity indicates that the stream function, Ψ_i, is a solution of (4) and satisfies both the normal and tangential boundary conditions at the body surface. Hence, proper definition of the problem allows for only one of the normal and tangential boundary conditions surface to be explicitly applied. In the current formulation, the normal component or no-penetration condition is used as the boundary condition and the tangential, no-slip condition is implicitly satisfied due to the representation of the internal kinematics of each solid body.

The relationship between the velocity and the vorticity is derived by the application of Green's Theorem to (1) for the flow region, *F*, and to (8) for the body region, B_i, combined through the boundary conditions (5) and (6). From this, the velocity field is calculated using the Biot-Savart law, which expresses the velocity in terms of the vorticity field. For a point *p* in the flow field, outside the solid region, the velocity is given by :

$$U_p = U_\infty + \frac{1}{2\pi}\int_F \omega \frac{\mathbf{k}\times(\mathbf{r}_p - \mathbf{r})}{\|\mathbf{r}_p - \mathbf{r}\|^2} dF + \int_{B_i} 2\Omega_i \frac{\mathbf{k}\times(\mathbf{r}_p - \mathbf{r})}{\|\mathbf{r}_p - \mathbf{r}\|^2} dB_i \qquad (9)$$

where the first term on the RHS represents the freestream velocity influence on the velocity at point *p* and the second term represents the influence of the vorticity in the flow field. The third term on the RHS is the induced velocity at point *p* by a velocity field with constant vorticity $2\Omega_i$, occupying the solid region B_i. This integral can be transformed into a surface integral along the boundary of the body, S_i, rather than an area integral (with respect to the body area dB_i), which enables a simplified evaluation of the moving boundary condition. This contribution to the velocity is due to the rotational motion of the body and is zero for the stationary objects considered in the present investigation.

The pressure distribution on the body surface can be evaluated by integrating the pressure gradient along the body contour. The pressure gradient at a point on the body surface is given by equation (10)

$$\frac{1}{\rho}\frac{\partial P}{\partial s} = -\mathbf{s}.\frac{D\mathbf{U}_c}{Dt} - \mathbf{n}.(\mathbf{r}-\mathbf{r}_c)\frac{D\Omega}{Dt} + \mathbf{s}.(\mathbf{r}-\mathbf{r}_c)\Omega^2 + \nu\frac{\partial\omega}{\partial n} \qquad (10)$$

where **s** and **n** are the tangential and normal vectors to the body surface. The first three terms on the RHS of (10) are due to the body motion and respectively represent the surface tangential components of the body reference point acceleration, the rotational acceleration and the centripetal acceleration. The final term is the negative rate of vorticity creation at the body surface and is calculated from the vorticity

distribution created in the control zone between time t-Δt and t (Sarpkaya, 1989). The resulting pressure distribution is integrated around the body surface to calculate the aerodynamic forces on the body and the moment about the body reference point at a particular timestep.

2.2. Mathematical modelling of the rivulet dynamics

Two-dimensional, unsteady flow of a thin film of incompressible viscous fluid with uniform dynamic viscosity, μ, and density, ρ, on the outer surface of a stationary horizontal circular cylinder of radius R is considered. This restricts all loading to act purely within the two-dimensional system defined and is in line with the previous numerical and analytical studies into aspects of RWIV (Matsumoto et al., 1992; Li and Gu, 2006; Lemaitre et al., 2007). In the initial analysis, the configuration under consideration is for the case when the windward direction is orthogonal to the component of gravity. Results presented later in the paper will consider the effect of varying the angle of attack in the plane due to the yaw and inclination of the cable.

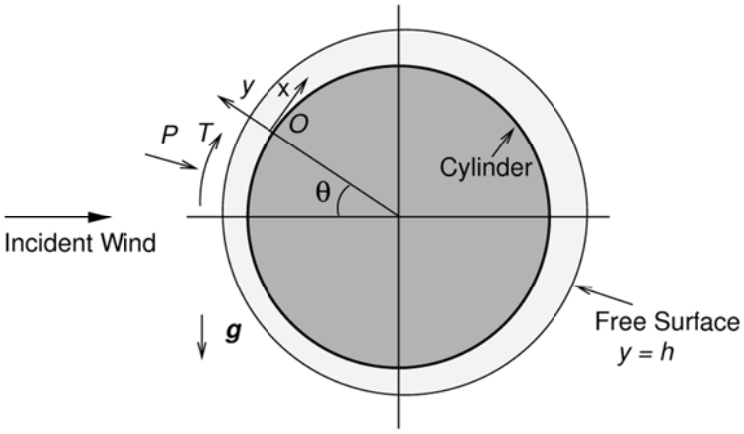

Figure 3. A thin fluid film on a horizontal cylinder.

As illustrated in Fig. 3, the free surface of the film coating the cylinder surface is subject to a prescribed pressure, $P = P(\theta, t)$, and a prescribed shear, $T = T(\theta, t)$, exerted by the external aerodynamic field. Both P and T are functions of the clockwise

angle from the windward (left-hand) horizontal, θ (0° ≤ θ ≤ 360°, Fig. 3) and time *t*. Using thin film theory, the evolution equation for the water thickness on the cylinder surface, $h(\theta, t)$, is given by

$$h_t + \left[-\frac{1}{3\mu R}\left(\rho g \cos\theta - \frac{\gamma}{R^3}\left(h + h_{\theta\theta}\right)_\theta + \frac{P_\theta}{R} \right) h^3 + \frac{Th^2}{2\mu R} \right]_\theta = 0 \ , \qquad (11)$$

where the subscripts denote differentiation. The full derivation of this evolution equation (11), along with verification of the approach, is given in Robertson et al. (2010). This equation is to be solved subject to an initial condition of the form $h(\theta, 0) = h_0(\theta)$, where $h_0(\theta)$ is the initial thickness of the water film. For the present work an initially uniform film thickness, h_0 = *constant*, has been used throughout and the film is allowed to evolve according to (11), to investigate the development of two-dimensional 'rivulets'. This evolution equation (11) is consistent with the corresponding equation given by Lemaitre et al. (2007) in the case of flow on a static cylinder and with an earlier equation (Reisfeld and Bankoff, 1992) for the case without aerodynamic loading. Given the nature of the problem, the same assumptions regarding the thin film and the boundary conditions were made here as were made in Lemaitre et al. (2007), and so the evolution equation (11) is essentially the same. However, unlike in the previous work, we present (11) in a dimensional rather than non-dimensional format, this being done to facilitate the coupling to the unsteady aerodynamic solver. Additionally, the results presented by Lemaitre et al. (2007) used constant aerodynamic loading rather than the time varying fully coupled approach utilised in the current research.

As the evolution equation (11) is a fourth order, non-linear, non-constant coefficient partial differential equation, it cannot, in general, be solved analytically. Therefore, a pseudo-spectral (or collocation) method solver using an *N*-point Fourier spectral mode in space and a fourth order Adams–Bashforth time-marching algorithm was constructed. This numerical method was chosen specifically because of the

periodic, continuous nature of the problem over the interval [0°, 360°) and the rapid rate of convergence it provides to the solution, given the presumed smoothness of the final result. The development of the numerical model and the results of a detailed validation and verification study investigating the effects of a static aerodynamic field on the rivulet evolution are presented in Robertson et al. (2010).

2.3. Coupled Numerical Solver

The unsteady aerodynamic solver, and the pseudo-spectral method solver for the water rivulet have been combined to form a coupled solver capable of predicting rivulet formation and evolution subject to an external aerodynamic field which they in turn influence. A flowchart displaying the basic operation of the coupled solver is displayed in Fig. 4, where DVM denotes the discrete vortex method aerodynamic solver. Experimental studies which consider the evolution of 'natural' rivulets have generally concentrated on ascertaining the conditions under which RWIV occurs and not on the exact form of these rivulets (Verwiebe and Ruscheweyh, 1998; Gu and Du, 2005; Flamand, 1995), though recent studies are beginning to provide more detailed information on the rivulet dynamics (Cosentino et al., 2003; Li et al., 2010). Therefore specific data against which to quantitatively verify either the coupled solver, or the results it predicts is unavailable, although qualitative comparison with experimental observations is possible.

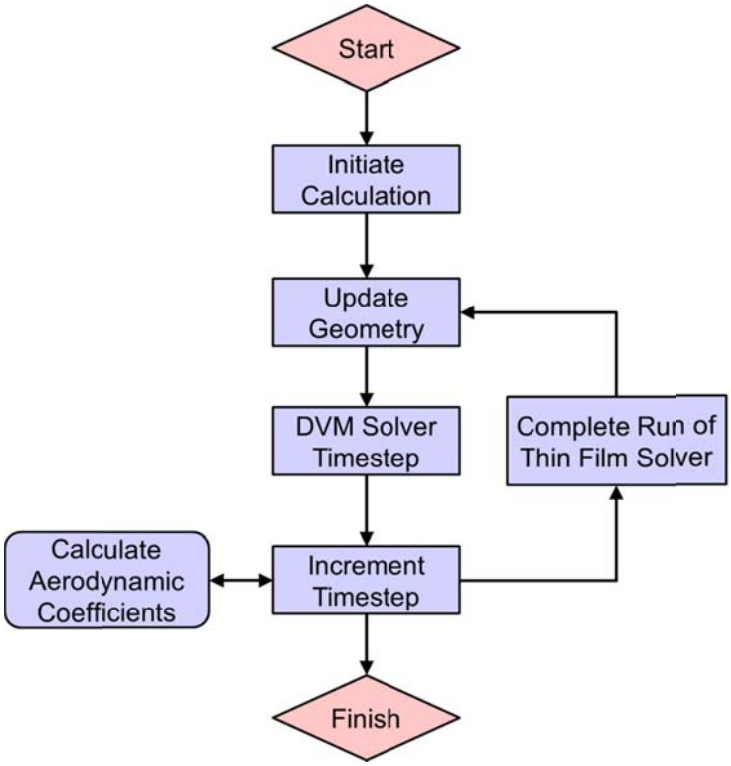

Figure 4. Simplified flowchart of the final coupled solver.

The values of the physical parameters used in the study are summarised below in Table 1. The Reynolds number was selected to be 1×10^5, chosen as it represented the mid-point of the typical range for RWIV, $0.5\times10^5 < Re < 1.5 \times 10^5$, as outlined earlier in the introduction. The cylinder is initially considered to be fully wetted with a film of equal thickness, with an initial film thickness, h_0, of 0.25×10^{-3} m. This particular value of the film thickness has been chosen to be consistent with the observations from experiments (Cosentino et al., 2003).

Parameter	Value
Cylinder radius, R	0.08 m
Initial film thickness, h_0	2.5×10^{-4} m
Gravity, g	9.806 m/s^2
Density of water, ρ_w	1000 kg/m^3

Dynamic viscosity of water, μ_w	1.002×10^{-3} Ns/m
Surface tension of water, γ	72×10^{-3} N/m
Density of air, ρ	1.19 kg/m^3
Dynamic viscosity of air, μ	1.82×10^{-5} Ns/m

Table 1. Values of the standard parameters used in the numerical calculation.

3. RESULTS FROM COUPLED SOLVER

3.1. Full Loading.

Given that the coupled solver is two-dimensional and that the governing evolution equation (11) was derived for a horizontal cylinder, the full loading case to be examined here essentially represents the physical loading on a horizontal cable perpendicular to the incoming flow, i.e. $\alpha = \beta = 0°$ (Fig. 1). A more complete discussion of the results from the coupled solver, for various loading cases is provided in Taylor and Robertson (2011) and only a summary of the full loading case for the horizontal cable presented herein. The evolutionary profile of film thickness around the surface of the cable is presented in Figs. 5 and 6, where Fig. 6 shows only the region close to the upper rivulet.

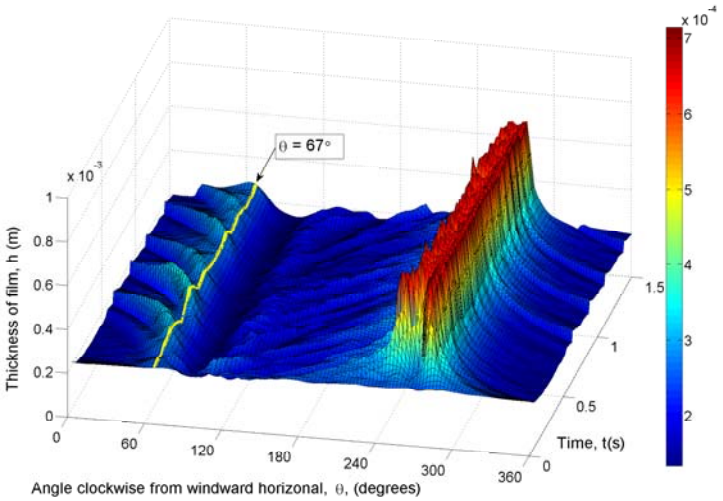

Figure 5. Numerical prediction of temporal evolution of film thickness in real time, under full loading.

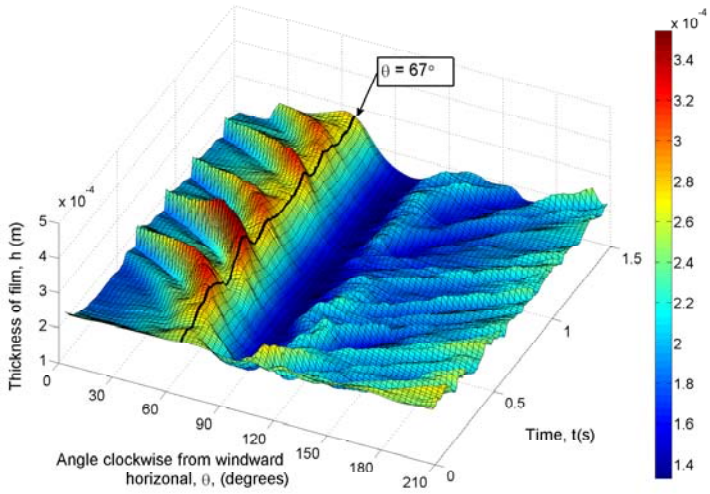

Figure 6. Numerical prediction of temporal evolution of film thickness close to the region of the upper rivulet in real time, under full loading.

The most noticeable feature of this result is the asymmetry of the rivulet evolution due to the effect of gravity, with very different rivulet profiles on the upper (0° – 180°) and lower (180° to 360°) surfaces of the cable. Compared to the results when gravity was omitted from the calculation (Taylor and Robertson, 2011) it is concluded that gravity has a stronger influence than either of the loadings due to the external aerodynamic field (pressure and shear), although these do still play a role. Whilst a distinct rivulet can be seen to form on the lower surface at approximately the lowest point on the cylinder, $\theta \simeq 277°$, the temporal evolution of the upper surface is more complicated and necessitates more detailed review. These two surfaces are therefore discussed separately.

The thickness of this lower rivulet is self-limiting, with a value of approximately 0.68×10^{-3} m, which is consistent with previous results (Taylor and Robertson, 2011) and is quantitatively in-line with the upper rivulet measured experimentally (Cosentino

et al., 2003). Furthermore as this rivulet forms on the lower surface, due to the effect of gravity this evolves more quickly than the previous aerodynamic only (no gravity) loading combinations examined (Taylor and Robertson, 2011). The location of this rivulet as defined by the point of maximum thickness has likewise moved leeward (towards the lowest point) due to the effect of gravity in comparison with the aerodynamic only cases.

While the lower rivulet is easy to distinguish, the evolution of the thin film on the upper surface is considerably more complicated. A small rivulet does periodically form on the upper surface at approximately $\theta = 67°$ (Figs. 5 and 6), before moving away in a 'rippling' motion due to the combination of aerodynamic and gravitational loading. A similar effect of rivulets periodically forming and moving around the cable surface is observed in recent wind tunnel experiments presented in Li et al. (2010) and Chen et al. (2013). The location at which rivulets are forming, $\theta = 67°$, is in the region previously determined to be danger for RWIV. From the artificial rivulets studies (Taylor et al., 2010; Matsumoto et al., 2007), this location is within the range of negative lift slope and may increase susceptibility to galloping and likewise, previous experimental studies have shown that rivulets in this location cause the largest cable response (Bosdogianni and Olivari, 1996; Gu and Du, 2005).

The thickness and location of this rivulet vary with time due to the rippling effect and is illustrated in Fig. 7 by tracking the variation in film thickness at $\theta = 67°$. By considering the time difference between the peaks in Fig. 7, also from spectral analysis, the period of formation of rivulets at $\theta = 67°$ can be determined as approximately 0.23 s (as previously reported in Taylor and Robertson, 2011 and Robertson, 2008). Interestingly this period is three times the period of Karman vortex shedding for this body, which is the same value that was found by Matsumoto et al. (2001) to play an important role in a high reduced velocity vortex-induced vibration

(HSV) phenomenon. Matsumoto et al. (2001) also indicates that the presence of rivulets on the cable surface seems to enhance the instability, illustrating some as yet undetermined link between HSV and the rivulets. Hence, the periodic appearance of this rivulet at an angular location that, as discussed above, is in the range that may cause instabilities, could prove to be a contributory factor to the underlying cause of the HSV phenomenon. As both flow features occur at the same frequency of $1/3f_s$, this observation may lead to an insight into the underlying mechanism that could link HSV to RWIV. However, this is only an initial observation and as the axial vortex previously identified (Matsumoto et al., 2001) as being of central importance to this is a three-dimensional flow feature it cannot be captured in the present 2D work. As such this conjectured link is very tentative. Further work to investigate any such link is a subject of future research projects and would require a fully 3D numerical approach.

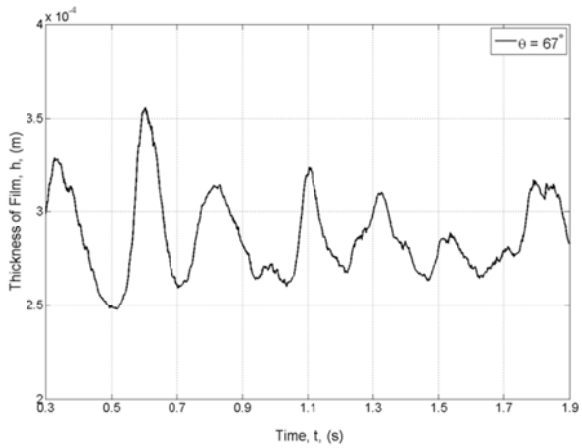

Figure 7. Temporal evolution of film thickness at a location 67° clockwise from the windward horizontal under full loading conditions.

3.2. Case Studies

Following on from the analysis of the full loading case, a series of further case studies were undertaken to establish the effect that specific parameters have on overall evolutionary response, and in particular on any rivulets which may form. Two such

studies examining initial film thickness on the cable surface, h_0, and the angle of attack in the plane normal to the cable axis, γ_θ, are presented and discussed herein.

3.2.1. Initial Thickness of Thin Film

A range of initial film thicknesses between 0.1×10^{-3} m ≤ h_0 ≤ 0.35×10^{-3} m were investigated to investigate the effect of thinner and thicker initial film thickness compared to the results presented in section 3.1 for an initial thickness of 0.25×10^{-3} m. As discussed earlier, the numerical simulations assume the cable is fully wetted with a uniform initial thickness of water. This is a simplifying assumption that has enabled a practical model to be successfully developed. In experiments where water is sprayed onto the cable and in full scale observations, the cable is usually not fully wetted and limited information is generally only available for the rivulet location not thickness. However, to ensure the simulations are a reasonable comparison with experiments, as indicated above, the datum initial water thickness was set to be 0.25×10^{-3} m which is comparable to the "base carpet" thickness of $0.2 - 0.25\times10^{-3}$ m as identified and measured experimentally by Cosentino et al. (2003). The range of film thicknesses studied in this research were chosen to be 0.1×10^{-3} m smaller and larger than this 'base carpet'. For consistency, in each case the initial profile was set to be uniform thickness, $h(\theta, 0) = h_0(\theta)$ = constant.

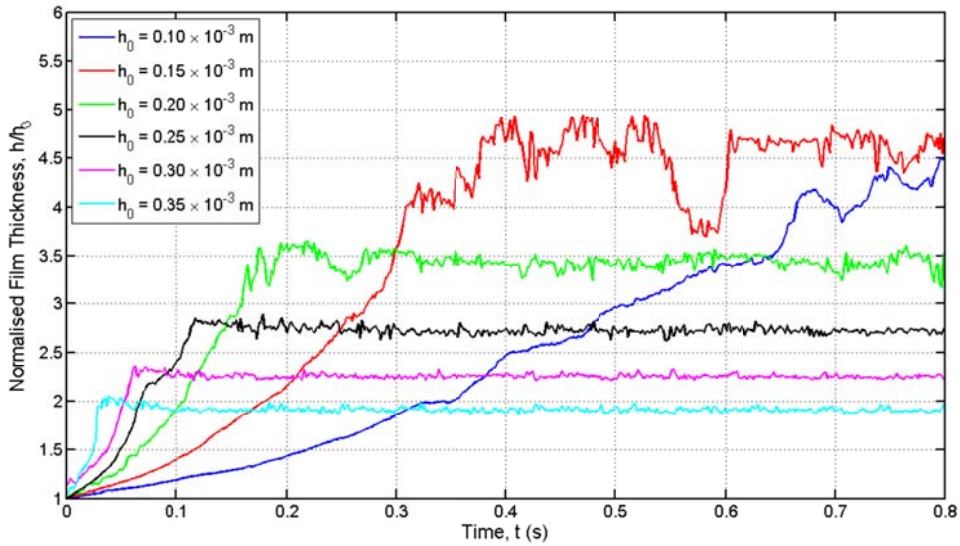

Figure 8. Temporal evolution of the normalised thickness of the lower rivulet for various initial thicknesses of film under full loading conditions. Variation of h/h_0 with t for different h_0.

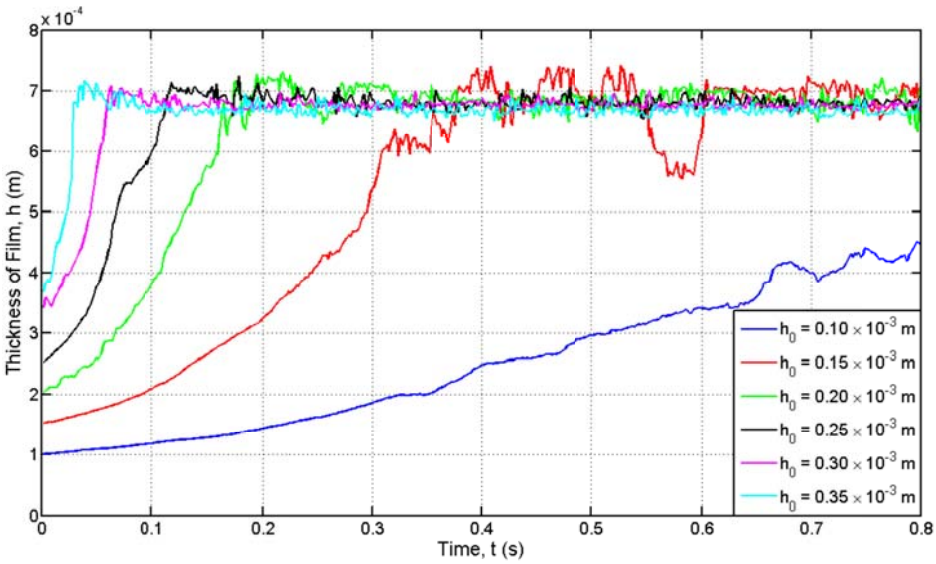

Figure 9. Temporal evolution of the thickness of the lower rivulet for various initial thicknesses of film under full loading conditions. Variation of h with t for different h_0.

The temporal evolution of the normalised and actual film thickness of the lower surface rivulet are presented in Figs 8 and 9 respectively. In each case, the normalised film thickness is with respect to the initial value, h_0. As the results in Fig. 8 illustrate, a distinct rivulet of self-limiting thickness does form in each case. Additionally, the lower rivulet forms at approximately the same mean location for each of the initial film thicknesses investigated, $\theta \cong 277°$. From Fig. 8, the time taken for the film to reach a self-limiting thickness varies, with the thicker films growing faster than thinner films. From Robertson et al. (2010), using thin film theory the velocity of the water film normal to the cable surface, in the absence of surface tension is given by

$$\hat{u} = -\frac{1}{2\hat{\mu}}\left(2\hat{\rho}g\cos\theta + \hat{p}_x\right)\left(2hy - y^2\right) + \frac{Ty}{\hat{\mu}} \qquad (12)$$

where the subscripts denote differentiation. At a particular thickness, the normal velocity of the free surface $\hat{u}$, can be derived by substituting the present thickness h into equation (12).

$$\hat{u} = -\frac{1}{2\hat{\mu}}\left(2\hat{\rho}g\cos\theta + \hat{p}_x\right)h^2 + \frac{Th}{\hat{\mu}} \qquad (13)$$

From Eq (13), it can be clearly seen that the normal velocity of the film, $\hat{u}$, and hence the growth rate of the terms corresponding to pressure and gravitational terms loading increases in proportion to the present free surface thickness squared (P and g $\propto h^2$), whereas the shear term only does so in direct proportion to the free surface thickness ($T \propto h$). As the normal velocity increases with film thickness, equation (13) clarifies why initially thicker films grow quicker than thinner films and why the rate of h/h_0 for any film increases with time (Fig. 8). Also, as the film becomes thicker, the growth rate (the gradient dh/dt) of that rivulet increases as can be seen in Fig. 9.

Interestingly the maximum self-limiting thickness of the lower rivulet was almost independent of the initial thickness of film. Figure 9 illustrates this for the first 0.75 s of evolution which is sufficient for all cases except the thinnest film, $h_0 = 0.1\times10^{-3}$ m, to

reach this state, which although not explicitly shown does so at approximately t = 1.3 s. The limiting thickness value of $h \cong 0.67\times10^{-3}$ m agrees well with those thicknesses obtained from the combinations of loading previously examined (Section 3.1, Taylor and Robertson, 2011), indicating that for the present conditions there was a maximum thickness of rivulet which could form before aerodynamic loading restricted further growth. The exact reasons for the particular limit are unclear as is whether or not this phenomenon is real or the result of one of the assumptions made herein. That said however, an examination of different cylinder radii did result in different maximum thicknesses in each case, this though was not the focus of the present investigation and is not reported here. Intuitively it makes sense that such a limit would exist for film thickness, just as a limiting wind speed for the actual formation of rivulets within RWIV has been previously reported (Cosentino et al., 2003; Matsumoto et al., 1992; Flamand, 1995; Verwiebe and Ruscheweyh, 1998). That the present value qualitatively matches that found experimentally by Cosentino et al. (2003) for the same diameter of cable provides some verification for the modelling approach used.

Because of the consistency of this self-limiting thickness and the condition for zero fluid flux, i.e. conservation of thin film area modelled, the actual evolutionary profiles once this limit is achieved are significantly different for the various initial film thicknesses studied. While the lower rivulets all have the same maximum thickness those which evolve from thinner films (smaller h_0) have significantly smaller base widths than those which form from thicker fluids (larger h_0). Figure 10 illustrates this at t = 1.4 s by which time all lower rivulets have ceased to increase in thickness. This figure also highlights that a rivulet was found to form on the upper surface ($0° < \theta < 180°$) for all initial thicknesses of film considered. While the actual thickness and location of this varied as it moved windward to join the lower rivulet, the mean location at which this formed was approximately constant, matching the base case of $h_0 = 0.25\times10^{-3}$ m

as θ ≅ 67° in all cases. As indicated in Fig. 10, the thickness of the film is rapidly changing between 65°-70° in all cases, consistent with the rivulet growth or formation in this location. Additionally, the peak thickness of the upper rivulet is consistent in all cases, located at between 50°-60°, thus illustrating the formation of the upper rivulet does not vary with initial film thickness.

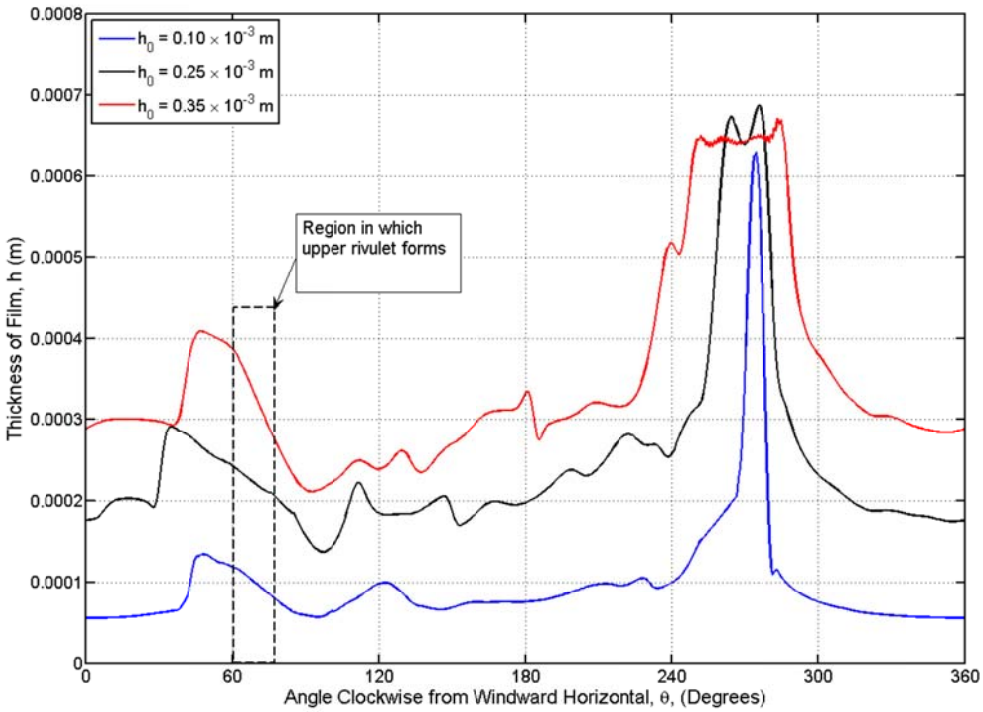

Figure 10. Comparison of film thickness profiles which result from various initial thickness of film under full loading conditions at a time of 1.4 seconds. Variation of h with θ for varying h_0 at t = 1.4 s.

A comparison of the evolution of the rivulets on the cable surface for h_0 = 0.15×10^{-3} m and h_0 = 0.3×10^{-3} m, is illustrated in Figs. 11 and 12 respectively. These results provide further confirmation of all the aspects of the water film evolution as discussed above. The slower growth rate of the lower rivulet for the thinnest film is clear, as is the self-limiting film thickness and the increased width of the rivulet in the

case with larger initial h_0. An additional aspect that is also noticeable in Figs. 11 and 12 is that the characteristic “ripples” arising from the upper rivulet are only present in the case with the thicker initial film, $h_0 = 0.3\times10^{-3}$ m. These ripples may eventually arise on the thinnest film thickness case, but due to the slower growth rate, would take much longer to form. The initial film thickness is therefore likely to influence the frequency at which these ripples form and drain towards the windward side of the cylinder. Earlier work noted the frequency of these ripples being similar to the frequency at which an enhanced Karman Vortex arises due to interactions with the axial vortex (Taylor and Robertson, 2011; Matsumoto et al., 2001). A moderate initial thickness of water is required for clear ripples to form, and it could be interpreted that this is consistent with full scale observations that “moderate” rainfall is required for RWIV to occur (Hikami and Shiraishi 1988). However, much more investigation is required before this can be accepted as a firm conclusion from these results.

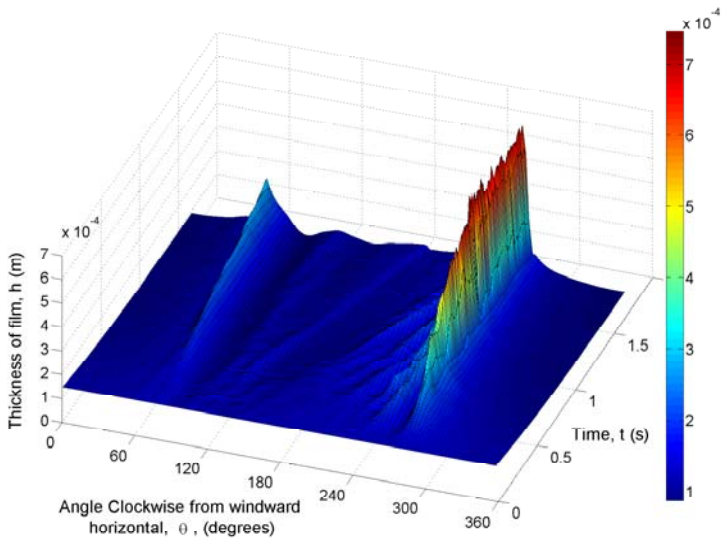

Figure 11. Numerical prediction of temporal evolution of film thickness in real time, with initial film thickness of 0.15×10^{-3} m. Variation of h with θ and t, where θ is measured clockwise from the windward horizontal.

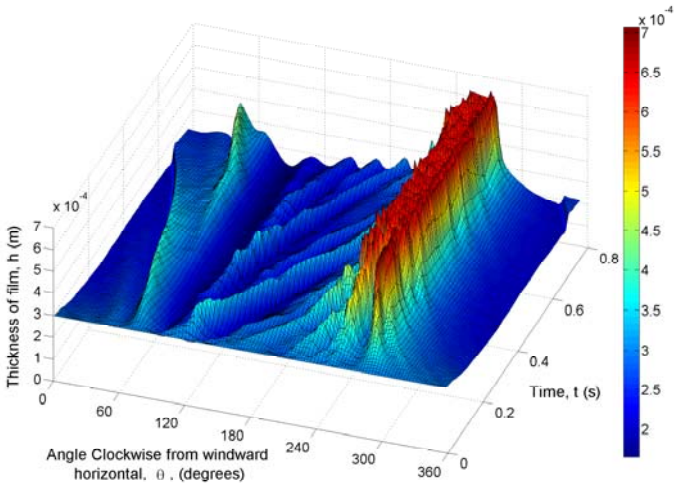

Figure 12. Numerical prediction of temporal evolution of film thickness in real time, with initial film thickness of 0.30×10^{-3} m. Variation of h with θ and t, where θ is measured clockwise from the windward horizontal.

3.2.2. Angle of Attack in Plane

The angle of attack in plane γ_θ (Appendix A) is a variable constructed such that the three-dimensionality of a yawed inclined cable can be represented in two dimensions (Fig. 13). If we assume the incident wind speed in plane U_{eff} and effective gravity g_{eff} remain fixed at the values for the full three-dimensional system (U and **g** respectively), as $\gamma_\theta = f(\alpha, \beta)$ this allows a range of angles of inclination and yaw to be examined by the variation of a single parameter. Using the typical limiting ranges for RWIV of $20° < \alpha < 45°$ and $20° < \beta < 60°$ outlined in section 1, a range of angles of attack in plane to be investigated could be established ($7° < \gamma_\theta < 51°$). To investigate the effect of varying angle of attack in plane, cases at 5° intervals of the range $10° < \gamma_\theta < 50°$ were thus investigated.

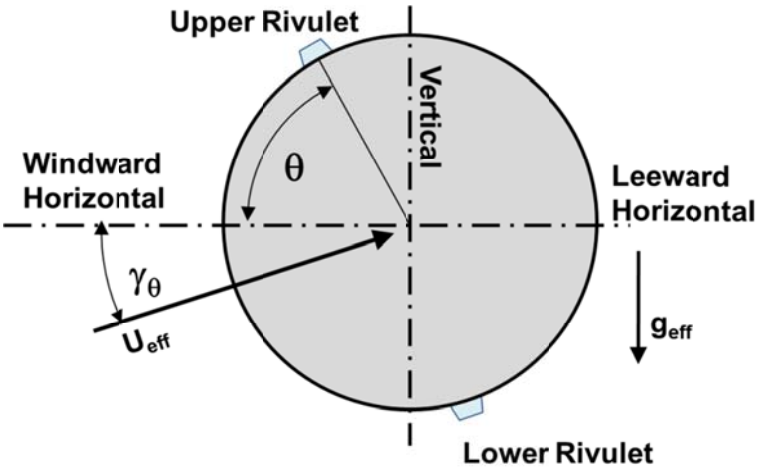

Figure 13. Schematic defining angle of attack in plane, γ_θ, and effective wind speed in plane, U_{eff}.

Consistent with the results presented earlier (section 3.1) for the horizontal cable (γ_θ = 0°), a large rivulet of self-limiting thickness was found to form on the lower surface for all values of γ_θ studied. Likewise 'ripples' were found to develop on the upper surface before moving circumferentially to join the lower rivulet, although whether or not an upper rivulet formed, was found to be dependent upon the angle of attack in plane. Figures 14 and 15 highlight the temporal evolution of one particular case, γ_θ = 20°, where an upper rivulet did form. These figures also illustrate that in this instance the lower rivulet formed was considerably narrower than the base case (Fig. 5) (γ_θ = 0°) and that this rivulet oscillates periodically by approximately θ ± 2° from its mean location θ = 265° (Fig 14). The variation in thickness and location of both the upper and lower rivulets with angle of attack in plane are now discussed in turn.

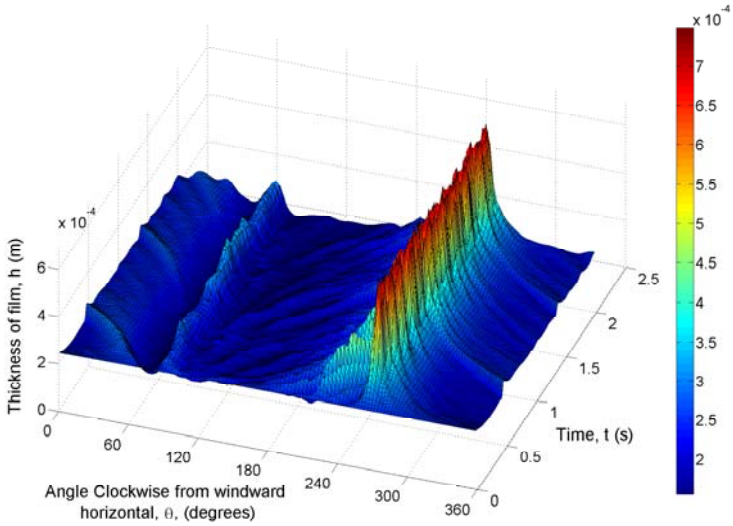

Figure 14. Numerical prediction of temporal evolution of film thickness in real time, under full loading conditions at γ_θ = 20°. Variation of *h* with θ and *t*, where θ is measured clockwise from the windward horizontal.

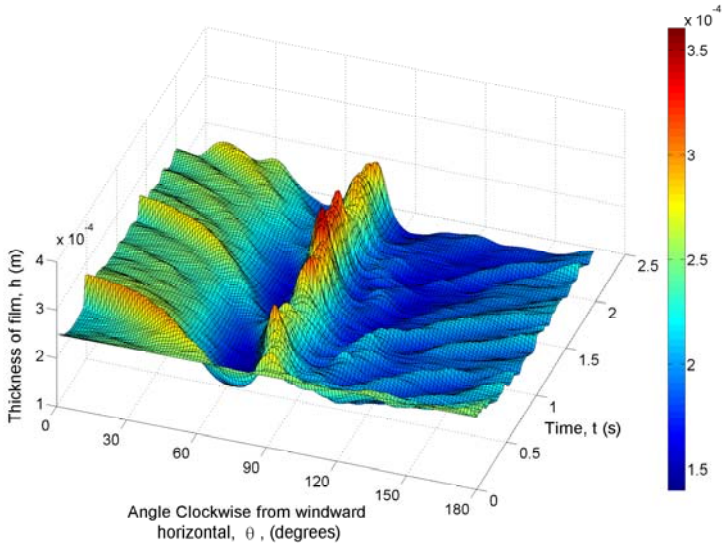

Figure 15. Numerical prediction of temporal evolution of film thickness close to the region of the upper rivulet in real time, under full loading conditions at γ_θ = 20°. Variation of *h* with θ and *t*, where θ is measured clockwise from the windward horizontal.

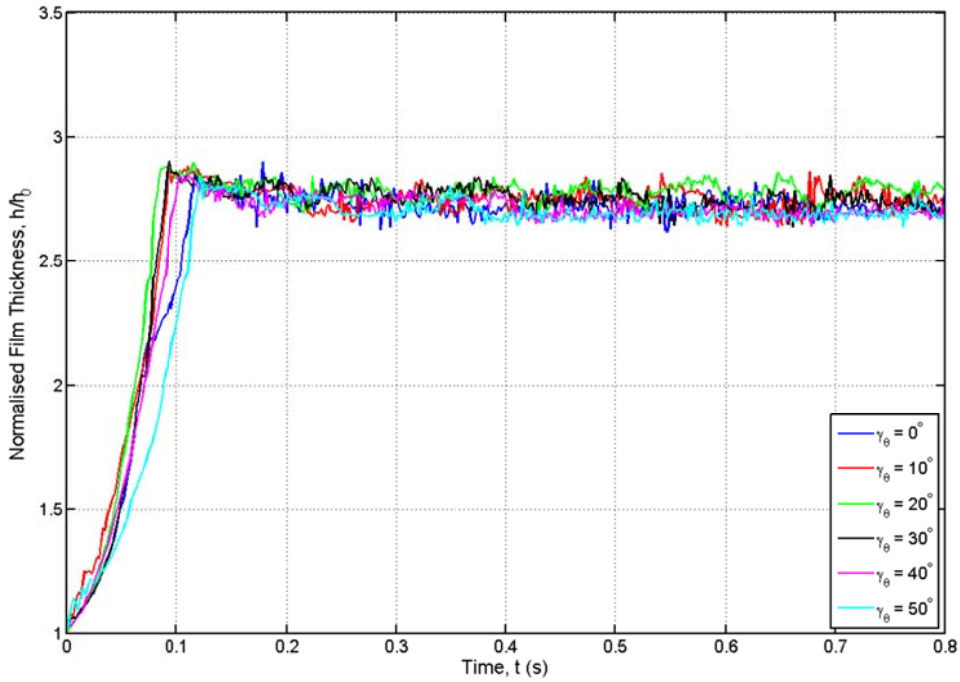

Figure 16. Comparison of temporal evolution of normalised film thickness of lower rivulet for various angles of attack in plane. Variation of h/h_0 with t for different at γ_θ.

Fig. 16 displays the variation in time of the normalised film thickness for different values of angle of attack in plane. As illustrated in the figure, the rate of growth and the self-limiting thickness of the lower rivulet in each case are very similar to both the base case ($\alpha = \beta = \gamma_\theta = 0°$) and to each other. It can therefore be said that when varied independently γ_θ has very little effect on either the thickness or the growth rate of the lower rivulet. It does however influence where this rivulet forms. For larger values of γ_θ, the component of aerodynamic loading directly opposing gravitational loading increases. This increase acts to 'blow' the rivulet further up the leeward face, as illustrated in Fig. 17. The mean location of the lower rivulet therefore varies with γ_θ, as can be seen from Fig. 18, where the location angle, θ_{ac}, is shown as anti-clockwise

from the horizontal. This figure also illustrates the range of oscillation about this mean location, which reaches a maximum at the γ_θ = 20° case as discussed above. Notably, for the range of angles above 35°, ($\gamma_\theta \geq 35°$) small periodic oscillations of the rivulet were no longer detected. These observations regarding the lower rivulet location and oscillation agree well with the experimental work of Wang et al. (2005), who detected a rivulet "which tends to be more influenced by the gravity force … running in an approximate straight line" that moved up the leeward face with increasing γ_θ (when the system is described in the present nomenclature). This is further evidence that the numerical solver presented herein captures fundamental characteristic features of the rivulets found to evolve during experimental study.

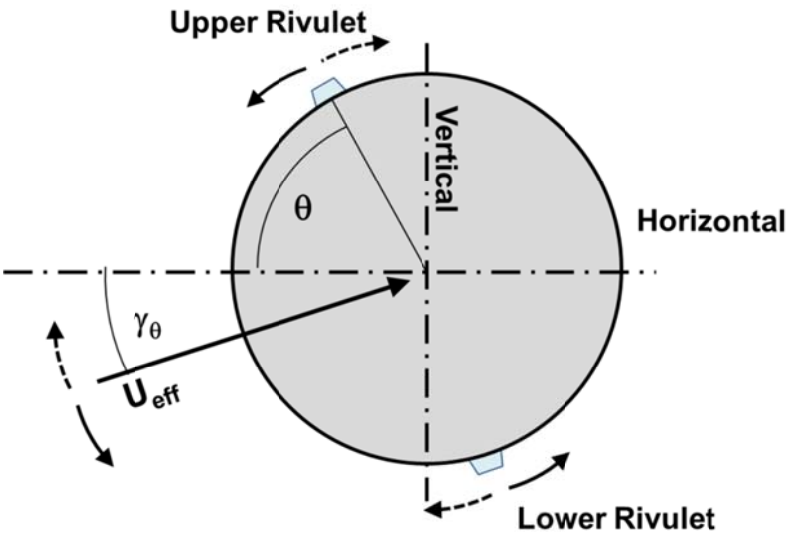

Figure 17. Schematic of effect that varying angle of attack in plane, γ_θ, has on rivulet location.

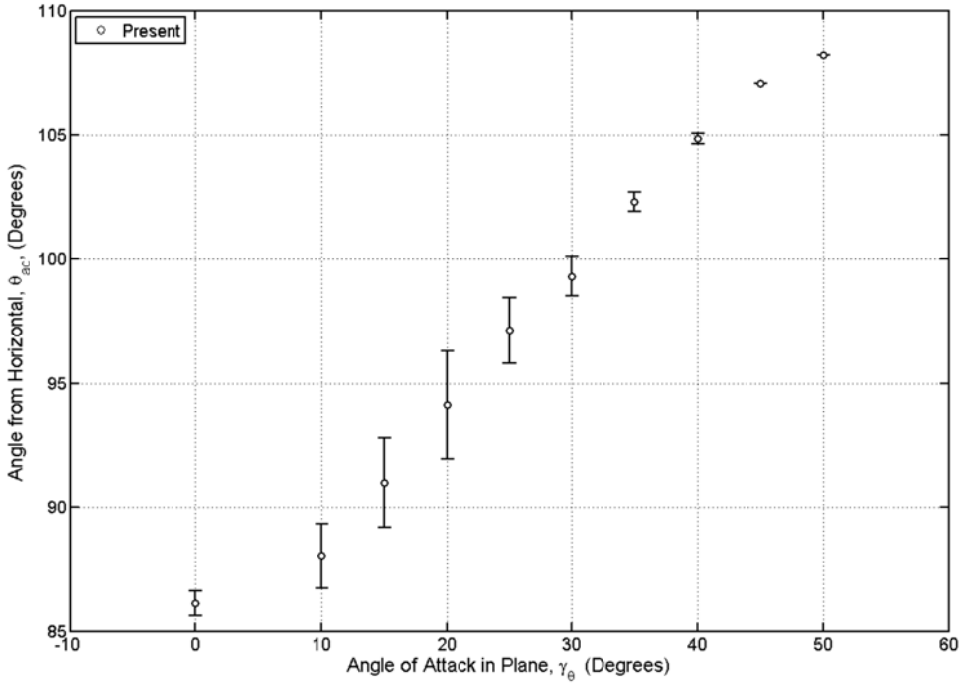

Figure 18. Comparison of location of mean location of lower rivulet and range of oscillation of this with angles of attack in plane. Variation of $\bar{\theta}_{ac}$ with γ_θ, where $\bar{\theta}_{ac}$ is measured ***anti-clockwise*** from windward horizontal.

For the cases at higher angle of attack, ascertaining a discernible pattern amongst the upper rivulets proves more complicated. This is illustrated in Fig. 19 which displays a magnified version of the upper surface of the water film evolution for of the γ_θ = 30° case. This can be compared to the similar result presented in Fig. 15 for the γ_θ = 20° case, and illustrates that once the angle of attack in plane reaches values of 30° or higher, no discernible upper rivulet could be detected although 'ripples' were still found on the surface. This can be ascertained by comparing Fig. 15 and 19 with the horizontal case (γ_θ = 0°) from Fig. 6. Both the γ_θ = 20° case (Fig. 15) and the γ_θ = 30° case (Fig. 19) show much smaller water thickness on the upper surface of the cylinder (0°<θ<180°), and a much less prominent formation of rivulets. However, in the

γ_θ = 20° case (Fig. 15), there is a clear ridge of water at about 80° around the cylinder, and some clear rivulets forming, though much less regular. Thus showing the rivulet formation is becoming less prominent but is still apparent. For the γ_θ = 30° case (Fig. 19) whilst there still is liquid moving down the windward face of the cylinder (θ decreasing from around 70°) or "ripples", there is a much less distinct pattern of rivulet formation, and the water thickness is generally much lower. The change between the three cases demonstrate that there is clear rivulet formation, moving down the windward face at low angle of attack in plane γ_θ, moving to a case where there is no clear pattern for γ_θ = 30°.

This may indicate a possible connection to the previous result (Fig. 18), as when no upper rivulet formed no oscillation of the lower rivulet could be detected. The present study could not establish such a link however. That said, the period of ripple formation was found to be constant at 0.23 ± 0.02 s in all cases which agrees well with the base case (γ_θ = 0°), as did the time interval between formation and these ripples joining the lower rivulet. However, this periodic phenomenon was found to be influenced by initial film thickness and thus, the effect of varying both initial thickness and angle of attack in plane is yet to be investigated.

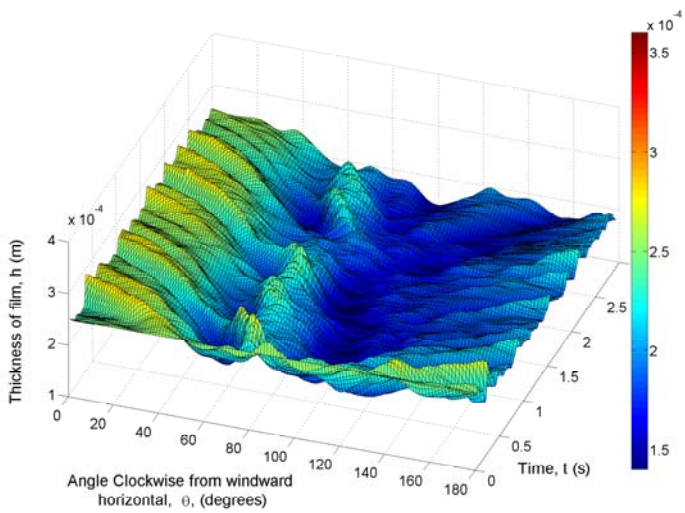

Figure 19. Numerical prediction of temporal evolution of film thickness close to the region of the upper rivulet in real time, under full loading conditions at γ_θ = 30°. Variation of *h* with θ and *t* where θ is measured clockwise from the windward horizontal.

As outlined earlier, the upper rivulet is thought to play a key role in RWIV mechanism. As such, the fact that these upper rivulets were only found to occur at $\gamma_\theta \leq$ 30° under the conditions examined herein, was thought to be an important result. Quantitatively this result is also in excellent agreement with results from experiments previously reported (Hikami and Shiraishi (1988); Flamand (1995); Gu and Du (2005); Zhan et al. (2008)). If the cable geometries and orientations under which RWIV has previously been detected in these prior experiments are transformed into the present notation, as presented in Table 2, oscillation was not found to occur at values significantly greater than γ_θ = 35°, consistent with the present results.

Experiment	Inclination, (α)	Yaw, (β)	Angle in plane, (γ_θ)
Hikami and Shiraishi (1988)	45°	45°	35.3°
Flamand (1995)	25°	30°	13.7°
Gu and Du (2005)	30° - 35°	25° - 40°	13.1° - 25.7°
Zhan et al. (2008)	30°	35°	19.3°

Table 2. Angles of inclination, yaw and angle of attack in plane at which previous experiments by Hikami and Shiraishi (1988), Flamand (1995), Gu and Du (2005) and Zhan et al. (2008) determined RWIV.

Furthermore in cases where an oscillating rivulet did form on the upper surface, while the mean maximum thickness of this rivulet $\bar{h}$ did not change significantly for $\gamma_\theta \leq$

25°, the mean angle $\bar{\theta}$ at which the rivulets originally formed did. This angle varied in such a manner as to maintain an almost constant angle between the location at which the rivulet originally formed and the stagnation point of the incident flow, $\gamma_\theta + \bar{\theta}$, as indicated in Table 3. The indication from this result is that the location of this upper rivulet is a direct consequence of the aerodynamic loading (Fig. 17). Table 3 also highlights the independence of mean maximum thickness of this upper rivulet with angle of attack in plane as well as the relation between γ_θ and $\bar{\theta}$. The latter of which is in good qualitative agreement with the experimental results of Bosdogianni and Olivari (1996) discussed earlier.

Angle of attack in plane, γ_θ.	Mean rivulet thickness, $\bar{h}$	Mean location of original rivulet formation, $\bar{\theta}$	Rivulet angle from stagnation, $\gamma_\theta + \bar{\theta}$
0°	0.30 mm	67°	67°
10°	0.31 mm	58°	68°
15°	0.30 mm	52°	67°
20°	0.29 mm	46°	66°
25°	0.28 mm	40°	65°

Table 3. Comparison of the mean maximum upper rivulet thickness $\bar{h}$, the mean location of formation $\bar{\theta}$ and the angle of formation from stagnation $\gamma_\theta + \bar{\theta}$ with angle of attack in plane γ_θ.

Spectral analysis of the lift coefficient for the various angle of attack in plane indicate that for angles < 30°, whilst there is a peak frequency corresponding to the Strouhal frequency, the magnitude is significantly lower than for the cases at angles ≥ 30°. Results of the spectral analysis for the γ_θ = 10°, 20° 30° and 35° cases are illustrated in Fig. 20. In the 10° and 20° cases, both indicate the main frequency

component of the lift coefficient is close to the expected Strouhal frequency of 0.2, with peak PSD values of 0.318 and 0.265 respectively. However, each signal demonstrates some characteristics of a broad band frequency response indicating that vortex shedding is not a dominant feature of the flow. In contrast, there is a much more dominant peak at a reduced frequency of 0.212 for the 30° case, with the peak value of the spectral density significantly larger than the other two cases (1.360 for the 30° case and 1.298 for the 35° case). In the 20° case the upper rivulet is much more discernible compared to the 30° case (Figs. 15 and 19) and despite the thickness still being very small, it will have a more significant effect on the external aerodynamic flow field. The presence of the rivulet in the 20° case will act as a trip on the external flow and will deflect the separated shear layer further from the centre line of the cylinder, thus causing a wider downstream wake. The wider wake reduces the interaction between the shear layers on either side of the cylinder, thus affecting the characteristics of the Karman vortex shedding. As there still is a significant frequency response at the Strouhal frequency, it cannot be stated that vortex shedding has been completely suppressed, but it has been greatly reduced. In contrast, this upper rivulet is not present in the 30 or 35° cases (Fig. 19), thus having a much lesser effect on the shear layer interaction and the Karman vortex shedding.

Previous research has indicated that when RWIV occurs, it does so at a much lower frequency than VIV and not in direct relation to the incident wind speed (Zuo et al. (2008); Hikami and Shiraishi (1988); Matsumoto et al. (2001)). Additionally, it has been reported by Matsumoto et al. (2001 and 2007), that suppression of vortex shedding is a characteristic necessary for galloping type oscillations. Previous research has also indicated that rivulets forming at around 67° from the stagnation means the cable is likely to be more susceptible to galloping type oscillations (Taylor et al., 2010; Matsumoto et al., 2007). As discussed above, the 20° case is in the region of yaw and inclination angles that are most likely to exhibit the RWIV phenomenon. The

results presented above, with upper rivulet formation at an angle from stagnation of 67° (Table 3) and the “suppressed” Karman vortex shedding (Fig. 20) are consistent with the previous findings. In general the results show consistency with previous experimental and full scale observations, and highlight aspects of the variation in the interaction between the external flow field and the water film that offer potential insights into the underlying physical mechanism of RWIV.

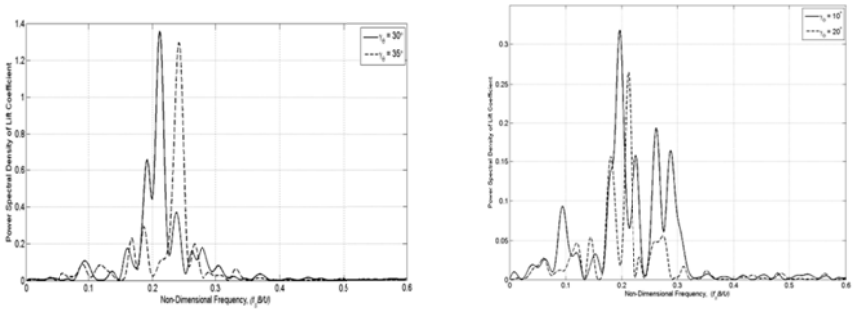

a) Angle in plane γ_θ = 30° and 35°

b) Angle in plane γ_θ = 10° and 20°.

Figure 20. Spectral analysis of full loading conditions at various angles of attack in plane.

4. CONCLUSIONS

A coupled model to investigate the Rain-Wind-Induced Vibration of cables has been developed. This utilizes an unsteady aerodynamic solver utilizing a vortex method approach together with a pseudo-spectral model to solve the evolution equation, for the water rivulet. This novel approach provides the most detailed simulations of the RWIV phenomenon to date.

Under aerodynamic and gravitational loading for a horizontal cylinder, a large lower rivulet was found to evolve with a self-limiting thickness. On the upper surface a small single rivulet was found to form periodically, before moving to join the lower rivulet under the actions of combined loading. The periodic nature of this rivulet is consistent with key mechanisms for RWIV previously identified.

Varying the initial thickness of the water film modified the growth rate of the lower rivulet, with the quickest growth rate found for the thickest initial thickness. However, the lower rivulet was again found to have a self-limiting thickness, the value of which was approximately the same in each case. The upper rivulet was found to form in each case but at very different growth rates. In addition, the presence and frequency of the rippling effect of the upper rivulet was dependent on the thickness, being more prevalent once the initial thickness was above about 0.25×10^{-3} m, consistent with previous observations that “moderate” rain is required for RWIV.

Varying the angle of attack in plane γ_θ allowed the three-dimensionality of a yawed inclined cable can be represented in two dimensions. The presence of the upper rivulet and its periodic formation were only present at angles of attach in plane of lower than 30°, which is in good agreement with previous experimental observations. In addition, at these angles, the Karman vortex shedding is significantly reduced, a consequence of which is that the cylinder is more susceptible to another aeroelastic instability. As these angles of attack in plane are in excellent agreement with those previously identified as causing the largest RWIV response (Gu and Du, 2005; Zhan et al. 2008) it can be concluded that rivulet formation and oscillation does indeed play a major role in the governing mechanism which underlies the RWIV phenomenon.

The successful prediction of characteristic features of RWIV, consistent with previous studies, provides excellent evidence of the capabilities of the present solver in tracking rivulet formation and evolution. It also highlights that this coupled solver has successfully taken the first steps towards numerically modelling RWIV and offers the opportunity to investigate detailed aspects of the aeroelastic phenomenon.

ACKNOWLEDGMENTS

The second author, Dr Andrew Robertson, gratefully acknowledges the support of the UK Engineering and Physical Sciences Research Council (EPSRC) via a Doctoral Training Account studentship. The support and collaboration of Prof. Stephen Wilson, Dr Brian Duffy and Dr Julie Sullivan, Department of Mathematics, University of Strathclyde, in deriving the evolution equation is gratefully acknowledged.

APPENDIX A : DERIVATION OF MODIFIED ANGLES

Two additional angles can be defined to help simplify the geometry of the three-dimensional yawed and inclined cable. Firstly the relative yaw angle, β^*, which defines the angle between the direction normal to wind and the cable axis. Secondly, the angle of attack in the plane normal to the cable axis, γ_θ, which is a variable constructed such that the three-dimensionality of a yawed inclined cable can be represented in two dimensions. This appendix provides derivations of analytical expressions for these two modified angles, illustrations of which can be seen in Figure A.1.

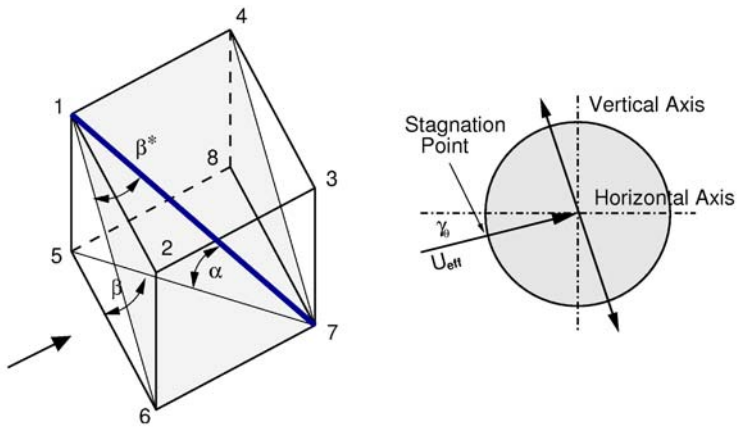

Figure A.1 : Definitions of angles α, β, β^*, U_{eff} and γ_θ, along with the numbering convention for vertices.

Derivation of Relative Yaw Angle

The incident wind speed, *U*, is parallel to sides 1-4, 2-3, 5-8 and 6-7. Assuming that this is horizontal, i.e. in plane 1-2-3-4 or 5-6-7-8, then, as illustrated in Fig. A.2, we can derive the components of the wind parallel and perpendicular to line 5-7 in this horizontal plane as

$$U \parallel U_{5-7} = U \sin\beta \quad \text{and} \quad U \perp U_{5-7} = U \cos\beta \qquad \text{(A.1)}$$

From these the velocity components parallel and perpendicular to line 1-7 in the plane 1-5-7 can be derived as

$$U \parallel U_{1-7} = U \cos\alpha \sin\beta \quad \text{and} \quad U \perp U_{1-7} = U \sin\alpha \sin\beta \qquad \text{(A.2)}$$

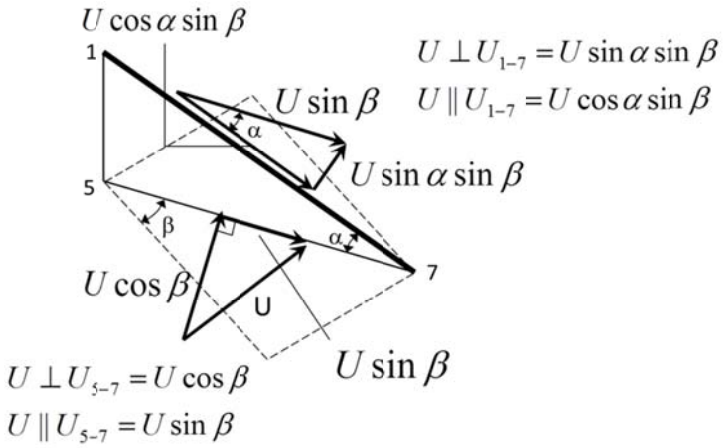

Figure A.2 : Components of velocity normal and perpendicular to cable plane and cable axis.

Therefore, β^*, defined as the angle between the direction normal to the wind and the cable axis (1-7) is given by (Fig. A.3),

$$\sin\beta^* = \frac{U \cos\alpha \sin\beta}{U} \qquad \text{(A.3)}$$

which can be simplified to

$$\beta^* = \arcsin(\cos\alpha \sin\beta) \qquad \text{(A.4)}$$

This is equivalent to the original definition given by Matsumoto et al. (1990), but in a slightly different notation which matches the more commonly used format that is given later in Matsumoto et al. (2001).

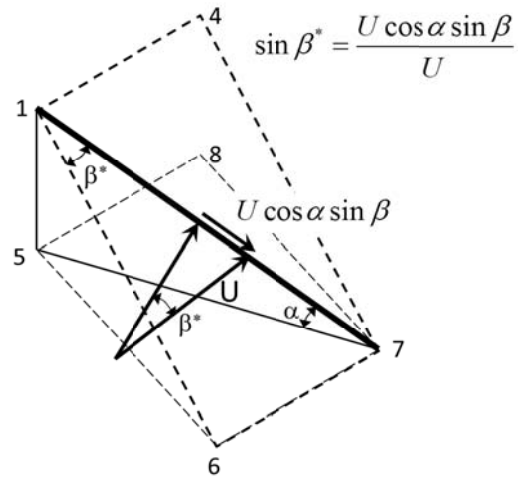

Figure A.3 : Definition of angle, β^*, between direction normal to the wind, and the cable axis.

Derivation of Angle of Attack in Plane

Using the derivations of the previous section an effective wind speed in the plane normal to cable axis, U_{eff}, can be determined from its perpendicular components (Fig A.4), as derived in (A.1) and (A.2) respectively. The effective wind speed in the plane can therefore be given as

$$U_{eff} = \sqrt{(U \perp U_{5-7})^2 + (U \perp U_{1-7})^2}$$
$$= U\sqrt{\cos^2\beta + \sin^2\alpha\sin^2\beta} \qquad \text{(A.5)}$$

From this a derivation of the angle between the stagnation point and the horizontal axis in plane outlined in Figures A.1 and A.4 can be derived as

$$\sin\gamma_\theta = \frac{U \perp U_{1-7}}{U_{eff}} = \frac{U\sin\alpha\sin\beta}{U\sqrt{\cos^2\beta + \sin^2\alpha\sin^2\beta}} \qquad \text{(A.6)}$$

Which can subsequently be simplified as

$$\gamma_\theta = \arcsin\left(\frac{\sin\alpha\sin\beta}{\sqrt{\cos^2\beta + \sin^2\alpha\sin^2\beta}}\right) \qquad \text{(A.7)}$$

This agrees with the definition given in Wilde and Witkowski (2003) and is equivalent to that originally developed by Matsumoto et al. (1990).

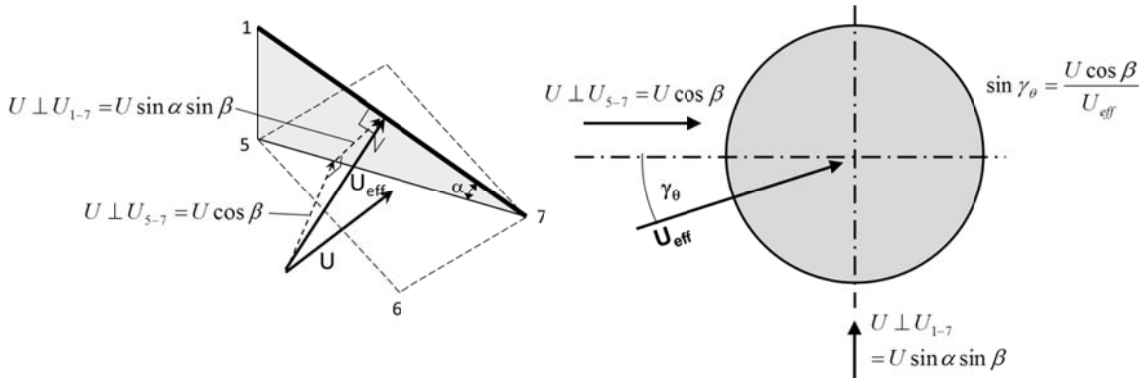

Figure A.4 : Definition of angle of attack in plane, γ_θ.

REFERENCES

Bosdogianni, A., Olivari, D., 1996. Wind and rain induced oscillations of cables of stayed bridges. J. Wind Eng. Ind. Aerod. 64(2-3), 171-185.

Chen, W.-L., Tang, S.-R., Li, H., Hu, H., 2013. Influence of dynamic properties and position of rivulet on rain-wind-induced vibration of stay cables. J. Bridge Eng. 18(10), 1021-1031.

Cosentino, N., Flamand, O., Ceccoli, C., 2003. Rain-wind induced vibration of inclined stay cables. Part I: Experimental investigation and physical explanation. Wind Struct. 6(6), 471-484.

Flamand, O., 1995. Rain-wind induced vibration of cables. J. Wind Eng. Ind. Aerod. 57(2-3), 353-362.

Geurts, C., Vrouwenvelder, T., Van Staalduinen, P., Reusink, J., 1998. Numerical modelling of rain-wind-induced vibration : Erasmus Bridge, Rotterdam. Struct. Eng. Int., IABSE 8(2), 129-135.

Gu, M., Du, X., 2005. Experimental investigation of rain-wind-induced vibration of cables in cable stayed bridges and its mitigation. J. Wind Eng. Ind. Aerod. 93(1), 79-95.

Gu, M., Huang, L., 2008. Theoretical and experimental studies on the aerodynamic instability of a two-dimensional circular cylinder with a moving attachment. J. Fluid. Struct. 24, 200-211.

Hikami, Y., Shiraishi, N., 1988. Rain-wind induced vibrations of cables in cable stayed bridges. J. Wind Eng. Ind. Aerod. 29(1-3), 409-418.

Lemaitre, C., Hemon, P., De Langre, E., 2007. Thin water film around a cable subject to wind. J. Wind Eng. Ind. Aerod. 95, 1259-1271.

Li, H., Chen, W.-L., Xu, F., Li, F.-C., Ou, J.-P., 2010. A numerical and experimental hybrid approach for the investigation of aerodynamic forces on stay cables suffering from rain-wind induced vibrations. J. Fluid. Struct. 26(7-8), 1195-1215.

Li, S.Y., Gu, M., 2006. Numerical simulations of flow around stay cables with and without fixed artificial rivulets. Proc. 4th Int. Symp. Comp. Wind Eng. (CWE2006), Yokohama, Japan, 16-19 July 2006, 307-310.

Lin, H., Vezza, M., Galbraith, R.A.McD., 1997. Discrete vortex method for simulating unsteady flow around pitching aerofoils. AIAA J. 35(3), 494-499.

Liu, Q., Matsumoto, M., Yagi, T., Hori, K., 2007. LES study on the mechanism of rain-wind induced vibration of cables of cable-stayed bridge. Proc. 12th Int. Conf. Wind Eng., Cairns, Australia 1-6 July 2007, 895-902.

Macdonald, J.H.G., Larose, G.L., 2008. Two-degree-of-freedom inclined cable galloping – Part 1 : General formulation and solution for perfectly turned system. J. Wind Eng. Ind. Aerod. 96, 291-307.

Matsumoto, M., Shiraishi, N., Kitazawa, M., Knisely, C., Shirato, H., Kim, Y., Tsujii. M., 1990. Aerodynamic behaviour of inclined circular cylinders-cable aerodynamics. J. Wind Eng. Ind. Aerod. 33, 63-72.

Matsumoto, M., Shiraishi, N., Shirato, H., 1992. Rain-wind induced vibration of cables of cable-stayed bridges. J. Wind Eng. Ind. Aerod. 41-44, 2011–2022.

Matsumoto, M., Saitoh, T., Kitazawa, M., Shirato, H., Nishizaki, T., 1995. Response characteristics of rain-wind induced vibration of stay-cables of cable stayed bridges. J. Wind Eng. Ind. Aerod. 57, 323-333.

Matsumoto, M., Yagi, T., Shigemura, Y., Tsushima, D., 2001. Vortex-induced cable vibration of cable-stayed bridges at high reduced wind velocity. J. Wind Eng. Ind. Aerod. 89(7-8), 633-647.

Matsumoto, M., Yagi, T., Goto, M., Sakai, S., 2003. Rain–wind-induced vibration of inclined cables at limited high reduced wind velocity region. J. Wind Eng. Ind. Aerod. 91, 1-12.

Matsumoto, M., Yagi, T., Adachi, Y., Hatsuda, H., Shima, T., 2007. Karman vortex effects on aerodynamic instabilities of inclined stay-cables. Proc. 12th Int. Conf. Wind Eng. Cairns, Australia, 175–182.

Ni, Y.Q., Wang, X.Y., Chen, Z.Q., Ko, J.M., 2007. Field observations of rain-wind-induced cable vibration in cable-stayed Dongting Lake Bridge. J. Wind Eng. Ind. Aerod., 95(5), 303-328.

Peil, U., Dreyer, O., 2007. Rain-wind induced vibrations of cables in laminar and turbulent flow. Wind Struct. 10, 83-97.

Reisfeld, B., Bankoff, S.G., 1992. Non-isothermal flow of a liquid film on a horizontal cylinder. J. Fluid Mech. 236, 167-196.

Robertson, A.C., 2011, Numerical simulation of rivulet dynamics associated with rain-wind induced vibration. PhD Thesis, University of Strathclyde, Glasgow, UK.

Robertson, A.C., Taylor, I.J., Wilson, S.K., Duffy, B.R., Sullivan, J.M., 2010. Numerical simulation of rivulet evolution on a horizontal cable subject to an external aerodynamic field. J. Fluid. Struct. 26, 50-73.

Ruscheweyh, H., Verwiebe, C., 1995. Rain-wind-induced vibrations of steel bars. Proc. Int. Symp. Cable Dyn., Liege, Belgium, October 1995, 469–472.

Sarpkaya, T., 1989. Computational Methods with Vortices - The 1988 Freeman Scholar Lecture. J. Fluid. Eng. – T. ASME 111(1), 5-52.

Taylor, I.J, Robertson, A.C., Wilson, S.K., Duffy, B.R., Sullivan, J.M., 2010. New developments in rain-wind induced vibrations of cables. P. I. Civil Eng. Str. B. 163(2), 73-86.

Taylor, I,J., Robertson, A.C., 2011. Numerical simulation of the airflow-rivulet interaction associated with the rain-wind induced vibration phenomenon. J. Wind Eng. Ind. Aerod. 99, 931-944.

Taylor, I.J., Vezza, M., 1999. Prediction of unsteady flow around square and rectangular cylinders using a discrete vortex method. J. Wind Eng. Ind. Aerod. 82(1-3), 247-269.

Taylor, I.J., Vezza, M., 2001. Application of a discrete vortex method for the analysis of suspension bridge deck sections. Wind Struct. 4(4), 333-352.

Verwiebe, C., Ruscheweyh, H., 1998. Recent research results concerning the exciting mechanism of rain-wind-induced vibrations. J. Wind Eng. Ind. Aerod. 74-76, 1005-1013.

Wang, Z.J., Zhou, Y., Huang, J.F., Xu, Y.L., 2005. Fluid dynamics around an inclined cylinder with running water rivulets. J. Fluid Struct., 21, 49–64.

Wilde. K., Witkowski, W., 2003. Simple model of rain-wind-induced vibrations of stayed cables. J. Wind Eng. Ind. Aerod. 91, 873-891.

Yamaguchi, H., 1990. Analytical study on growth mechanism of rain vibration of cables. J. Wind Eng. Ind. Aerod.33, 73-80.

Zhan, S., Xu, Y.L., Zhou, H,J., Shum, K.M., 2008. Experimental study of wind-rain-induced cable vibration using a new model set up scheme. J. Wind Eng. Ind. Aerod. 96, 2438-2451.

Zuo, D, Jones, N.P., 2003. Interpretation of observed damper performance in mitigating wind and rain-wind-induced stay-cable vibrations. Proc. 11th Int. Conf. Wind Eng., Lubbock, Texas, USA, June 2003, 2133-2140.

Zuo, D., Jones, N.P., Main, J.A., 2008. Field observation of vortex- and rain-wind-induced stay-cable vibrations in a three-dimensional environment. J. Wind Eng. Ind. Aerod. 96, 1124-1133.